Crack path in liquid metal embrittlement: experiments with steels and modeling

T. Auger
CentraleSupelec/MSSMAT, UMR CNRS 8579, Grande voie des vignes, Chatenay-Malabry, France
thierry.auger@centralesupelec.fr

S. Hémery
ISAE–ENSMA, Institut Pprime, UPR CNRS 3346, département "Physique et mécanique des matériaux", ENSMA, Téléport 2, 1, avenue Clément-Ader, BP 40109, 86961 Futuroscope Chasseneuil-du-Poitou cedex, France
samuel.hemery@ensma.fr

M. Bourcier
CentraleSupelec/MSSMAT, UMR CNRS 8579, Grande voie des vignes, Chatenay-Malabry, France
math31@hotmail.com

C. Berdin
University of Paris Sud/ICMMO, CNRS UMR 8182, Orsay, France
clotilde.berdin@u-psud.fr

M. Martin
Institute für Materialphysik, Georg-August Universität Göttingen, Germany
lmartin@ump.gwdg.de

I. Robertson
University of Wisconsin-Madison, Wisconsin, United States of America
irobertson@wisc.edu

ABSTRACT. We review the recent experimental clarification of the fracture path in Liquid Metal Embrittlement with austenitic and martensitic steels. Using state of the art characterization tools (Focused Ion Beam and Transmission Electron Microscopy) a clear understanding of crack path is emerging for these systems where a classical fractographic analysis fails to provide useful information. The main finding is that most of the cracking process takes place at grain boundaries, lath or mechanical twin boundaries while cleavage or plastic flow localization is rarely the observed fracture mode. Based on these experimental insights, we sketch an on-going modeling strategy for LME crack initiation and propagation at mesoscopic scale.
At the microstructural scale, crystal plasticity constitutive equations are used to model the plastic deformation in metals and alloys. The microstructure used is either extracted from experimental measurements by 3D-EBSD (Electron Back Scattering Diffraction) or simulated starting from a Voronoï approach. The presence of a crack

within the polycrystalline aggregate is taken into account in order to study the surrounding plastic dissipation and the crack path. One key piece of information that can be extracted is the typical order of magnitude of the stress-strain state at GB in order to constrain crack initiation models. The challenges of building predictive LME cracking models are outlined.

KEYWORDS. Crack path; Liquid Metal Embrittlement; Steels; Multi-scale crack propagation modelling.

INTRODUCTION

Liquid metal embrittlement (LME) is the transition from ductile to brittle fracture when a metallic material is stressed in contact with a liquid metal. In spite of decades of studies, mostly by macro-scale experiments, but also down to the atomic scale (in particular by high resolution transmission electron microscopy on grain boundaries), this phenomenon is still fundamentally not well understood. While many investigations have focused on "model-systems" such as Cu/Bi, Ni/Hg or Al/Ga, LME is also observed with steels where this phenomenon has received much less attention despite its considerable practical importance (fission or fusion cooling systems). One reason is that the phenomenology with steel's LME is often obscured by the specific physico-chemistry details of each system or by the technical difficulties due to the requirements of high quality testing at high temperature. Nevertheless, among today's critical topics in LME, the assessment of potential crack paths at the microstructural scale is a highly important piece of missing information. The insight based on synthesis of literature data is unclear, especially regarding steels. Whereas intergranular cracking is the most common case in LME [1] [4], cleavage and quasi-cleavage have been identified in steels as well [2][3] Up to recent time, the investigations of the fracture modes were limited to scanning electron microscopy or TEM of surface replicas [5]. However, complex microstructures of industrial alloys, such as martensitic steels, make the crack path identification difficult using conventional fractography tools, thereby leading to misidentification of the crack path as discussed in [6]. One key finding in this later work was the explanation of the unusual fracture surface as resulting from interlath cracking in plane stress loading condition. It was at the same time found that interlath cracks can be arrested by carbide precipitation at interlaths. Meanwhile, it was shown that interlath cracking is clearly enhanced, and correspondingly so is LME susceptibility, when the carbide distribution is modified such that carbides are depleted at the lath boundaries [7]. This implies that not only knowledge about the atomic scale mechanism is required but also a detailed mesoscopic understanding is crucially important for a correct understanding of LME's occurrence and the definition of sound strategies for LME's mitigation.

The present study mainly focuses on steels to highlight that there is a common fracture mode induced by liquid metals. To do so, fracture of martensitic, ferritic and austenitic steels in liquid sodium have been studied to assess the common denominator in the crack path for these cases. Various embrittling liquid metals are used to show the universality involved in steel's LME. Once one has clearly established LME's main crack path characteristics, one can proceed with the modeling of LME crack propagation. We sketch an on-going modeling strategy for LME crack initiation and propagation at mesoscopic scale.

At the microstructural scale, crystal plasticity constitutive equations are used to model the plastic deformation in metals and alloys. The microstructure used is either extracted from experimental measurements by 3D-EBSD (Electron Back Scattering Diffraction) or simulated starting from a Voronoï generated aggregate. The presence of an intergranular crack within a polycrystalline aggregate can be taken into account in order to study the surrounding plastic dissipation and the crack path. One key piece of information that can be extracted is the typical order of magnitude of the stress-strain state at the GB in order to constrain crack initiation models. Different fracture criteria can then be discussed. The challenges of building predictive LME cracking models are outlined.

CRACK PATH IN LME

Experimental

T91 martensitic steel, AISI 1010 ferritic-pearlitic steel and AISI 304L austenitic steel are sensitive to LME as shown in [3, 6, 8-10]. As a consequence, those steels have been selected for study of the LME crack path as a function of the microstructure. The compositions of the steels are shown in Tab. 1. Standard heat treatment of T91 steel

(austenitization then tempering at 750°C) results in a tempered martensite microstructure with prior austenitic grain size of 20µm. A much finer lath structure is present inside those grains with typical lath width of about 500nm. AISI 304L steel have been hyperquenched to obtain a 30 µm austenitic grained microstructure. Finally, AISI 1010 steel was tested in a near equilibrium ferrite-pearlitic state. The ferrite grain size was about 20 µm. All steels were tested in high purity liquid sodium to study the influence of the microstructure on the crack path. To assess the LME crack path as a function of the liquid metal species, indium, sodium, and lead bismuth eutectic (LBE) have been used on T91 steel. This steel is known to be sensitive to LME in various liquid metals [3, 6, 11].

Steel	C	Cr	Mo	V	Nb	S	Mn	P	Ni	Si
T91	0.08 – 0.12	8.00 – 9.50	0.85 – 1.05	0.18 – 0.25	0.06 – 0.10	0.01	0.3 – 0.6	<0.032	<0.4	0.2 – 0.5
1010	0.08 – 0.12	-	-	-	-	<0.05	0.3 – 0.6	<0.04	-	-
304L	<0.03	18 - 20	-	-	-	<0.03	<2.0	<0.045	8 - 12	<0.75

Table 1: Specification in composition of T91, AISI 1010 and 304L steels (wt %)

Round notched tensile specimens were used in sodium. The specimen diameter was 4 mm with a gage length of 15 mm. The notch was 500 µm deep with an angle of 60°. In indium and LBE, center cracked tensile (CCT) specimens were used. The specimen thickness was 1.5 mm (plane stress condition). The total width of the CCT specimens was 50 mm for a notch length of 10 mm. Specimens were heated by Joule effect in an inert gas atmosphere. The temperature was maintained for a 10 min period prior to testing to ensure a homogeneous temperature along the gauge length. A pyrometer ensures a control of the temperature with an accuracy of +/- 5K. The embrittling liquid, brought in small quantity at the notch before testing, melts by conduction and follows the crack by capillarity during the test due to good wetting. The temperature set during the tensile test was selected to ensure high embrittlement intensity above the melting temperature of the embrittling metal. In the case of sodium, crosshead displacement rate was chosen to limit the vaporization of the liquid metal in order to ensure its presence at the crack tip during the whole test duration. Temperatures and displacement rates are mentioned for every case studied. Due to its high reactivity, tests in sodium are performed under a high purity argon atmosphere (oxygen content <5ppm and moisture content <20ppm). Further details about the test procedure are given in [9] for sodium tests and in [6] for indium and LBE tests.

Since wetting is known to be a critical requirement for LME, specific preparation procedures are required before testing to promote wetting at the notch. Sodium wetting was improved by introducing pre-exposure steps in sodium at temperatures in the range 723 K – 823 K for 50h to 200h. Limited corrosion influence is expected in these conditions and further details about the sodium pre-exposure can be found in [8][9]. For indium and LBE, the notch of the CCT specimens is wetted with the help of a soft soldering flux mainly composed of zinc chloride, ammonium chloride after mechanical and electro polishing.

Given the differences in microstructural states, different investigation scales and tools had to be used to properly identify the crack path. Therefore, although scanning electron microscope (SEM) was used for conventional fractography to extract the crack path from fracture surfaces, Electron BackScattered Diffraction (EBSD) and Transmission Electron Microscopy (TEM) were also used to investigate crack propagation in finer low angle misorientation microstructures.

Before characterization of the fracture surfaces, the liquid metal needs to be removed. Sodium is eliminated in ethanol; LBE is dissolved in a mixture of acetic acid, hydrogen peroxide, and ethanol known to not affect the fracture surface; indium is removed by amalgamation with mercury at room temperature followed by ultrasonic cleaning in distilled water. Scanning Electron Microscopy observations were carried out using a LEO 1530. To assess the crack path next to the surface, some fractured samples were plated with gold followed by a 100 µm thick nickel electrodeposit allowing preparing cross sections by mechanical polishing. An un-plated sample cross section was also prepared using mechanical grinding followed by polishing using a JEOL Cross-Polisher. EBSD orientation maps were then acquired with a TSL Digiview4 camera using the OIM acquisition software. Some TEM samples containing arrested cracks were also extracted from broken T91 specimens using a Focused Ion Beam (FIB). The samples tested in sodium have been characterized using STEM imaging and transmission EBSD at 30kV in a Helios 660 FEI FIB. TEM analysis was performed on samples tested in liquid LBE and indium using an automated indexing of the diffraction pattern (ASTAR® analysis system) using a JEOL 3010-LaB6 operated at 300 kV.

Influence of the microstructure

To assess the role of the microstructure on the crack path, austenitic, ferritic-pearlitic and martensitic steels have been tested in liquid sodium on axi-symetrical tensile specimens at a temperature of 573 K under argon atmosphere. The crosshead displacement rate has been adjusted in relation to the total elongation during testing to avoid complete vaporization of sodium before the end of the test. The ductility of the materials being different and LME sensitivity being higher at low strain rates, 1010 and T91 steels were tested using a crosshead displacement rate of 0.015 mm/min whereas 304L steel was tested at 0.025 mm/min. Each of the selected test condition resulted in a brittle fracture of the specimen initiating from the notch and propagating over a total length of several hundred microns. To test the innocuity of the environmental exposure only, some specimens were pre-exposed to liquid sodium for long durations equivalent to those of the mechanical tests to be carried out in sodium. The remaining sodium was then removed in ethanol in order to carry out reference tests under argon atmosphere. Conventional fractography showed a ductile fracture behavior of this pre-exposed material when failed in the absence of liquid metal, showing the requirement of the presence of the liquid metal to cause embrittlement.

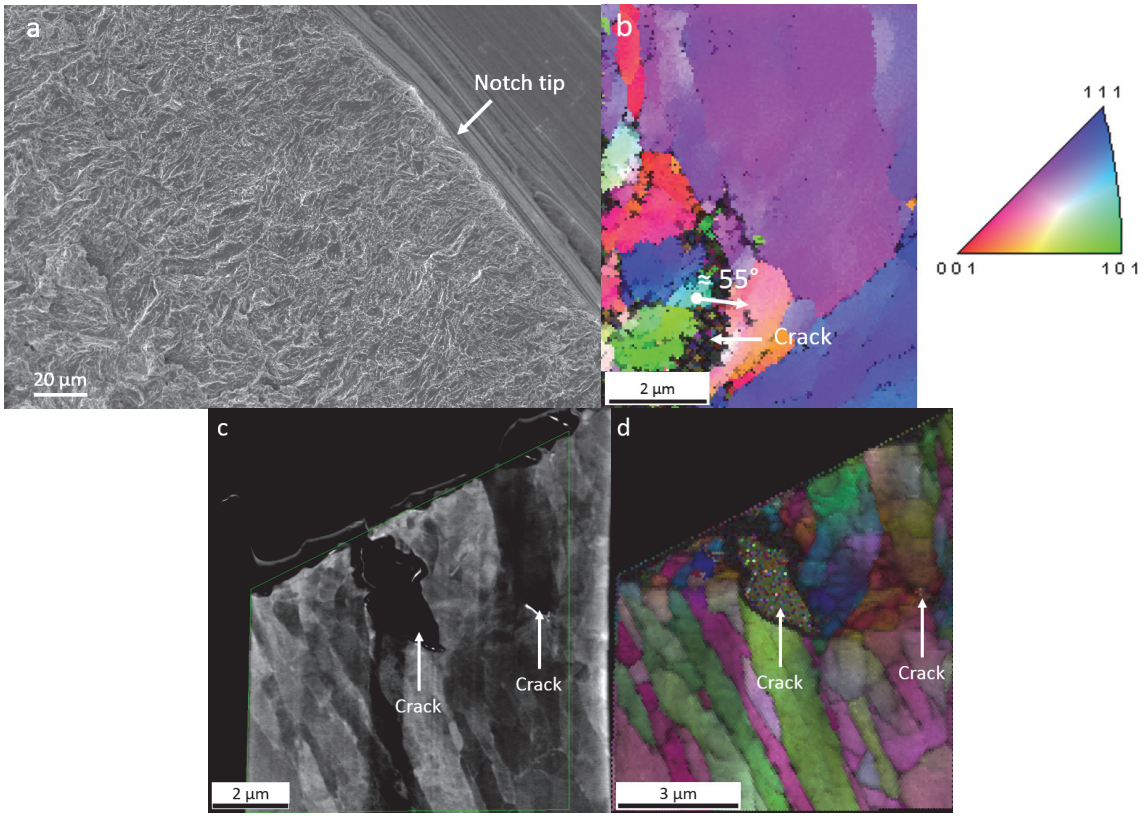

Figure 1: a. SEM micrograph of the brittle fracture surface near the notch tip of a T91 specimen tested in sodium, b. Crystalline orientation map of the microstructure surrounding an arrested crack obtained by conventional EBSD, c. Bright field STEM micrograph of a FIB machined sample, d. Orientation map of the microstructure surrounding arrested crack obtained by transmission EBSD.

SEM observations of the fracture surface of the T91 specimen tested in sodium at a crosshead displacement rate of 0.015 mm/min show an ubiquitous flat fracture surface. A SEM micrograph of the fracture surface is shown in Fig. 1a. The flatness confirms the brittle behavior of the material as observed in [9]. According to the observations and since the mean prior austenitic grain size is 20µm, prior austenitic grain boundaries do not seem to constitute a preferential crack path. In the conventional language of fractography, it is often referred as quasi-cleavage fracture surface. To properly identify the fracture mode either as cleavage or interlath cracking, finer crystallographic investigations were carried out. EBSD mapping on transverse cut sample prepared using a JEOL Cross-Polisher was performed in areas containing arrested

cracks to characterize the surrounding microstructure. A representative orientation map is shown in Fig. 1b. Despite a small misorientation expected from the opening of the crack, fracture is obviously intercrystalline. Misorientations profile measurements confirm this conclusion and show large step across the crack area typical of lath packet misorientation. Additional data was obtained from transmission EBSD of TEM samples containing an arrested crack. The bright field STEM image of the microstructure surrounding the crack is shown in Fig. 1c. The corresponding crystalline orientation map of the microstructure surrounding the arrested crack obtained by transmission EBSD is shown in Fig. 1d. It confirms the intergranular crack path for liquid sodium embrittlement of T91 steel.

AISI 304L specimens were tested at 573 K for a crosshead displacement rate of 0.025 mm/min. According to SEM observations at low magnification of the fracture surface, a flat ring extends starting from the notch towards the center of the specimen over several hundreds of microns. These features were absent from the reference specimen tested under argon without sodium, hinting at the occurrence of LME for this steel. Given the mean grain size (30μm), SEM combined with the EBSD technique was used to assess the crack path. The SEM fractography revealed a complicated fracture surface where the crack path is difficult to link with microstructural features as shown in Fig. 2a. A typical orientation map on a cross-section is shown in Fig. 2b. The observed cracks, corresponding to the deep trenches on the fracture surface, are clearly intergranular. The conclusion for the remaining areas is less clear; due to the large amount of plastic strain visibly experienced next to the fracture surface, martensite and mechanical twins are observed but, while not excluded, we have so far no indication that a preferential crack path is constituted by the austenite ferrite interface or by mechanical twins.

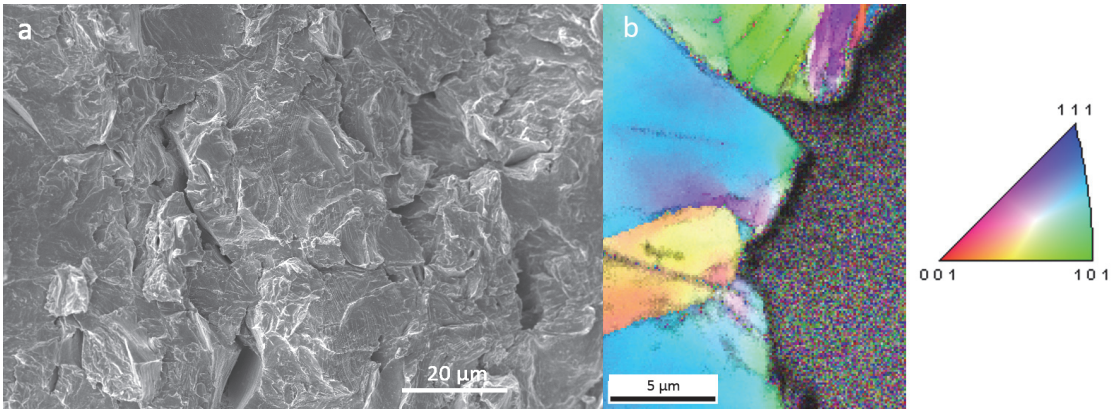

Figure 2: a. SEM micrograph of the brittle fracture surface near the notch tip of a AISI 304L specimen tested in sodium, b. Orientation map of the microstructure surrounding an arrested crack

AISI 1010 specimens were tested in sodium at a crosshead displacement rate of 0.015 mm/min and a temperature of 573 K. Conventional SEM here was sufficient to reveal flat area of brittle aspect extending from the notch tip over hundreds of microns. Several areas on the fracture surfaces clearly show intergranular cracking. One of them is shown in Fig. 3. Elsewhere, pearlite, with its numerous interfaces, and plastic strain makes the identification of the crack path more difficult. Overall, it reveals the occurrence of LME as already found by Hilditch et al. on a ferritic-pearlitic steel [10].

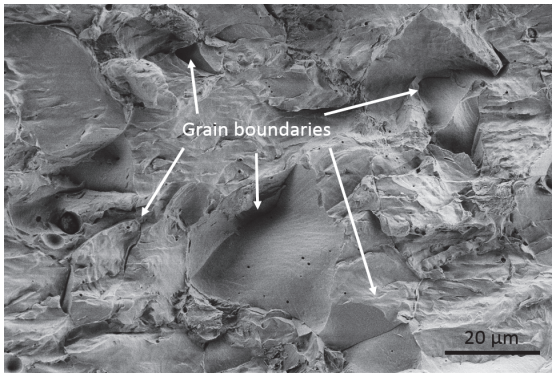

Figure 3: SEM micrograph of the brittle fracture surface of an AISI 1010 specimen tested in sodium

Influence of the liquid metal species

The role of the microstructure on LME crack path has been described with results in sodium liquid metal. A common potential intergranular or interlath crack path is found. One would like to know whether the crack path is similar with different liquid metals as well.

Results of LME of T91 by sodium, indium and lead-bismuth eutectic (LBE) are gathered here. This steel was selected instead of AISI 1010 or AISI 304L steels because of the good knowledge about some practical aspects related to LME such as wetting by liquid metals. Despite differences in the wetting procedures and testing triaxiality (axisymetrical notched tensile geometry versus center cracked tensile geometry for indium and LBE), the conclusions are believed not to depend upon these minor details. The brittle crack path in T91 induced by liquid sodium has been already described in the previous section. Therefore, only indium and LBE induced cracking will be discussed in the following.

Centre cracked tensile specimens were tested in contact with indium at 433 K and with LBE at 473 K. The tests were performed at constant crosshead speed (equivalent to 10^{-4} s^{-1} strain rate ahead of the crack tip). SEM observations of the fracture surface reveal a brittle fracture mode, indicating the occurrence of LME. Similarly to the case of liquid sodium embrittlement, prior austenitic grain cannot be easily distinguished. The characteristic length scale seems one order of magnitude smaller. To perform investigations at the lath scale, TEM samples were extracted from areas with arrested cracks using FIB [6]. TEM observation of the samples reveals the microstructure surrounding the arrested crack as shown on the bright field micrograph presented in Fig. 4a (sample fractured in LBE). Automatic index of the diffraction pattern was performed on the microstructure neighboring the crack using the ASTAR® analysis system. The corresponding orientation map given in Fig. 4b shows an interlath fracture mode. A similar procedure was applied to the sample fractured in indium. The result is shown in Fig. 4c. Here too, interlath fracture path interpretation is supported by misorientation profile measurements performed across the crack throughout the entire cracked area.

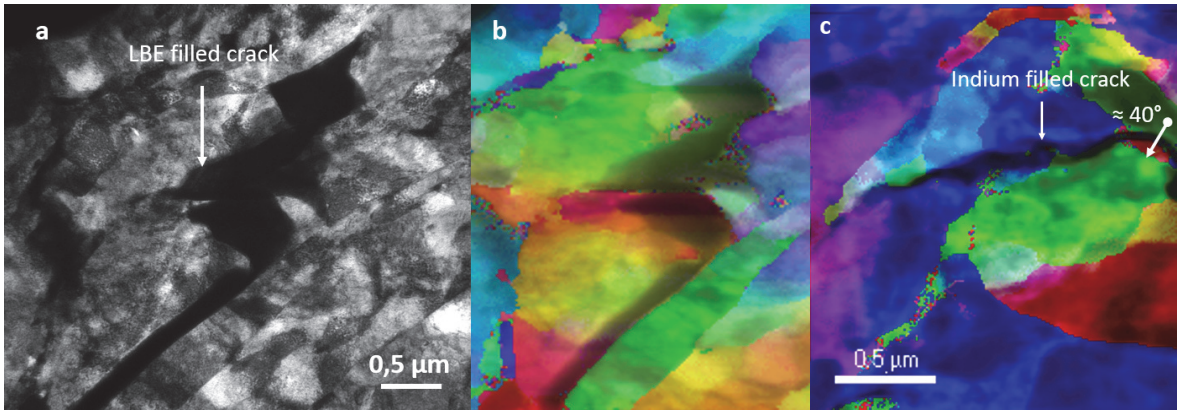

Figure 4: a. Bright field TEM micrograph of the microstructure surrounding an arrested LBE filled brittle crack, b. orientation map corresponding to the area shown in Fig. 4a, c. Transmission EBSD orientation map of an indium filled arrested crack

We do not exclude that dynamic recovery may occur in AISI 1010 even at the temperature used (≈0.3 Tf). One of the remaining questions would be whether or not in-situ formed subgrain boundaries may experience LME cracking. AISI 304L steel is also known to be in a metastable state. Indeed, martensite and mechanical twins have been observed next to the fracture surface. Nor is it excluded that newly created (in-situ) interfaces could constitute a preferential crack path, strengthening our point developed here. Indeed, LME is known to be sensitive to the structure of the grain boundary [12]. As a conclusion for this part, every LME case should be investigated using an extensive fractography work extending down to the nanoscale to properly identify the crack path. Intergranular or interlath cracking has been identified without doubt in every case studied. There remain unidentified features on the fracture surfaces (AISI 304L and AISI 1010 in liquid sodium notably) and we adopt a conservative point of view that it comes from fast linking between larger preexisting intergranular cracks through some lowest energy paths or dissipation processes. It can thus be considered that there is a common crack path encountered in LME of steels. As a consequence, numerical modeling of steel's LME has to involve liquid metal grain boundary decohesion rather than transgranular cracking as a starting point.

SKETCH OF THE MODELING OF A CRACK PROPAGATION IN LME

Having established the generic intergranular/interlath crack path character of steel's LME, one wishes to model crack propagation into a framework able to take into account the polycrystalline aspect of real materials, the large plasticity observed before cracking in LME and potentially various specificities of the onset of cracking such as a cracking criterion that could be tuned to the specific environment under consideration. It requires one to incorporate grain boundaries (GB), 3D shapes of grains and a set of assembled grains forming an aggregate to represent the 3 dimensional aspect of a material as close as possible to a representative element volume. Realistic grains to neighbouring grains crystallographic relationships need to be incorporated as well in order to represent not only the texture of a material but to correctly assess the micromechanics near GBs. The plastic behavior of such a material is then modeled via a finite element implementation of crystalline plasticity. Debonding at GBs can be obtained through the contact formulation of a finite-element solver using a dedicated LME fracture criterion.

3D agregate modeling

There are 2 possible ways to model 3D microstructures:

- The first one is to generate virtual microstructures representative of an equiaxed microstructure, for example, by using the Voronoï tessellation technique to define the grain morphology and grain size distribution [13]. The advantage is the ease with which one can generate a virtual microstructure. The generation of grain orientation might not be representative of the local misorientation (especially if the orientation is selected randomly) but can be made representative of the crystallographic texture through constrained selection.
- The other possibility is to use a 3D reconstruction of a real microstructure using either tomography by X-ray analysis [14] or destructive serial-sectioning by EBSD [15]. In this case, every material requires its own aggregate with a sufficient number of grains to be representative.

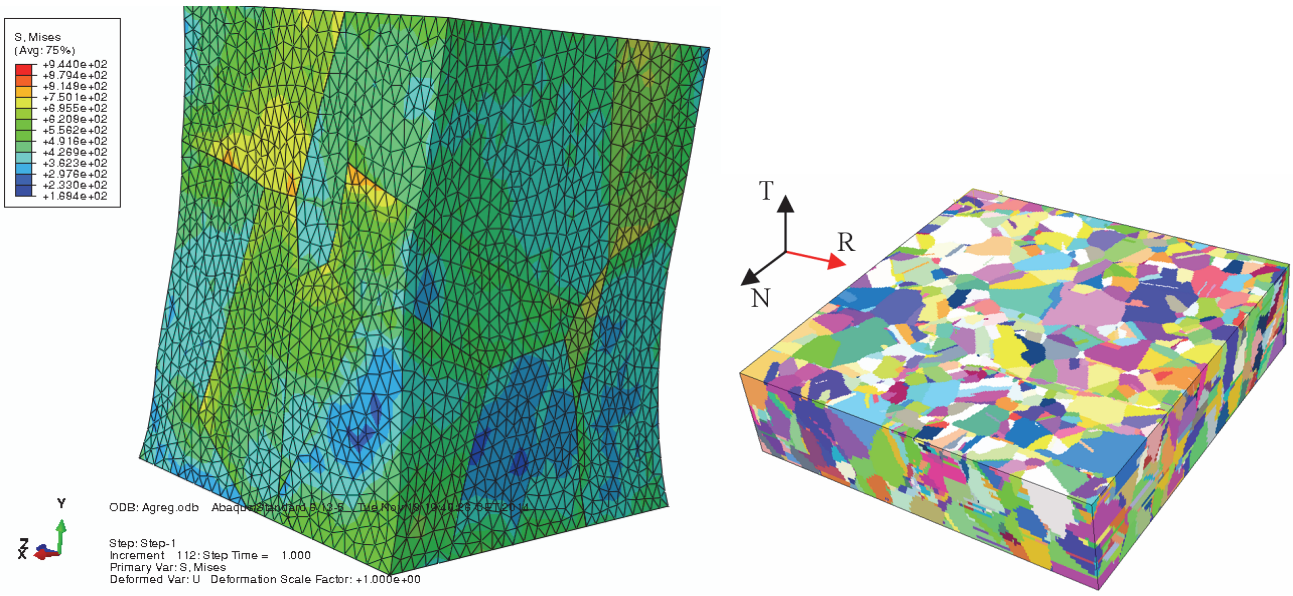

Figure 5: a. Deformed 3D-voronoï aggregate generated using Neper [13] b. 3D-EBSD aggregate obtained by serial sectioning on 316LN [16]

The boundaries are meshed using triangular elements. The volume mesh is created from the boundary surface with tetragonal (C3D4) elements.

Crystalline plasticity

The modeling of a material's polycrystalline plasticity is carried out in the framework of finite transformations (small elastic distortions but large lattice rotations) following the kinematic decomposition proposed by Pierce et al [17] for single crystals. Crystal plasticity constitutive equations are used to model the plastic deformation in metals and alloys [18].

The approach is implemented in the Abaqus® finite element code, using a UMAT (User MATerial) subroutine [19]. The plasticity criterion is given by the Schmid law: $\left|\tau^s\right| = \tau_c^s$ where $\tau^s = \left(\tilde{\tau}.\vec{n}^s\right)\vec{g}^s$ is the reduced shear stress on the glide plane (s) and τ_c^s is the local critical shear stress. At each time increment of the computation, we assume that the local critical shear stress is given by:

$$\tau_c^s = \tau_0^s + \mu b\sqrt{\sum_{u=1,12} a^{su}\rho^u} = \sum_u h^{su}\gamma^u$$

where μ is the isotropic shear modulus, b the norm of the Burgers vector, τ_0^c the lattice friction stress, h^{su} the component of the hardening matrix. The critical shear stress is a function of the components a^{su} of the interaction matrix (forest hardening) between the systems (s) and (u). The glide velocity $\dot{\gamma}^s$ is expressed with a classical viscoplastic potential based on the resolved shear stress and the critical shear stress for glide activating on system (s):

$$\dot{\gamma}^s = \dot{\gamma}_0\left(\frac{\left|\tau^s\right|}{\tau_c^s}\right)^n \text{ sign }(\tau^s) \quad \text{if} \quad \left|\tau^s\right| > \tau_c^s, \quad \dot{\gamma}^s = 0 \quad \text{otherwise}$$

where $\dot{\gamma}_0$ is a reference shear rate and n is the rate exponent. The dislocation density evolution is governed by a dislocation production term, based on Orowan's relationship, and is balanced by an annihilation dislocation term which takes into account the dynamic recovery during deformation:

$$\dot{\rho}^s = \frac{\left|\dot{\gamma}^s\right|}{b}\left[\frac{\sqrt{\sum_{u\neq s}\rho^u}}{K} - 2y_c\rho^s\right]$$

$2y_c$ is a material parameter related to an annihilation distance of dislocations. The first term corresponds to the inverse of the average mean free path of the statistically stored dislocations on the system (s). K is a material parameter.
Each material requires the identification of more than 20 parameters to be able to capture the plastic behavior shown in Fig. 6a. The modeling of such an aggregate allows the calculation of local strain and stress fields as well as the GB decohesion local stress.

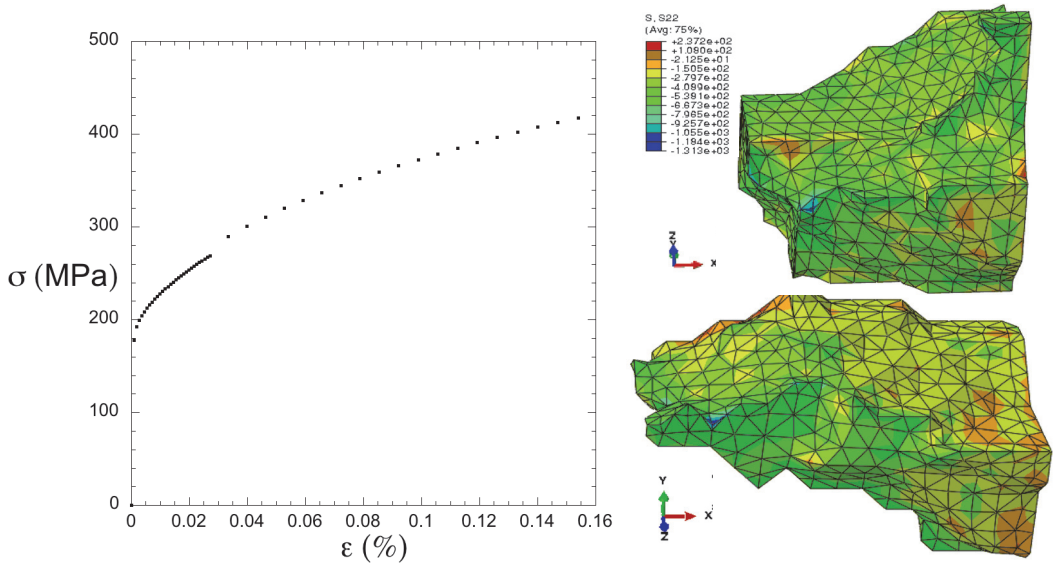

Figure 6: a. True stress versus true strain curve with 316LN parameters of the 3D aggregate Fig. 5b. b. S_{22} on 2 matching grains after 15% deformation along the Y direction (each of them is rotated oppositely by 30° around the x axis to be able to display the interface loading).

Perspective : 3D agregate modeling with a crack

A crack can be introduced in a polycrystalline model using the contact formulation (surface on surface contact). The local stress intensity factor can be calculated from the contour integration of the J integral. In Fig. 7, we show preliminary results on a 3 grain aggregate loaded with an initial crack. Crack propagation could be carried out after a fracture criterion based of the calculation of K $(K = \sqrt{EJ} > K_G)$ decides which part of the microstructure is to be broken.

Perspective : Fracture criterion for LME

There is currently no theoretical framework able to describe the ductile to brittle transition seen in LME. As a starting point one can use the Griffith theory of brittle fracture [20] that connects the macroscopic fracture energy to a microscopic quantity the surface energy γ_s via the critical stress intensity factor (SIF) for cracking K_G. It equates the energy release rate during the advance of a pre-existing crack (the drop in the stored elastic energy) to the energy cost required for the creation of two opposing surfaces. The minimum immediately gives the critical stress intensity factor for fracture (SIF):

$$K_G = \sqrt{\frac{4\mu\gamma_s}{1-\nu}} \quad , \text{ with } \nu \text{ the Poisson factor and } \mu \text{ the shear modulus}$$

The adsorption of a liquid lowers the surface energy, in most cases, such that, as a general rule, there should be a lowering of the critical SIF for brittle cracking [21]. The search of a critical K_c for cracking compatible with experiment would allow the calculation of an effective γ_s to be compared with a hypothetical measurement or calculation by atomistic methods.

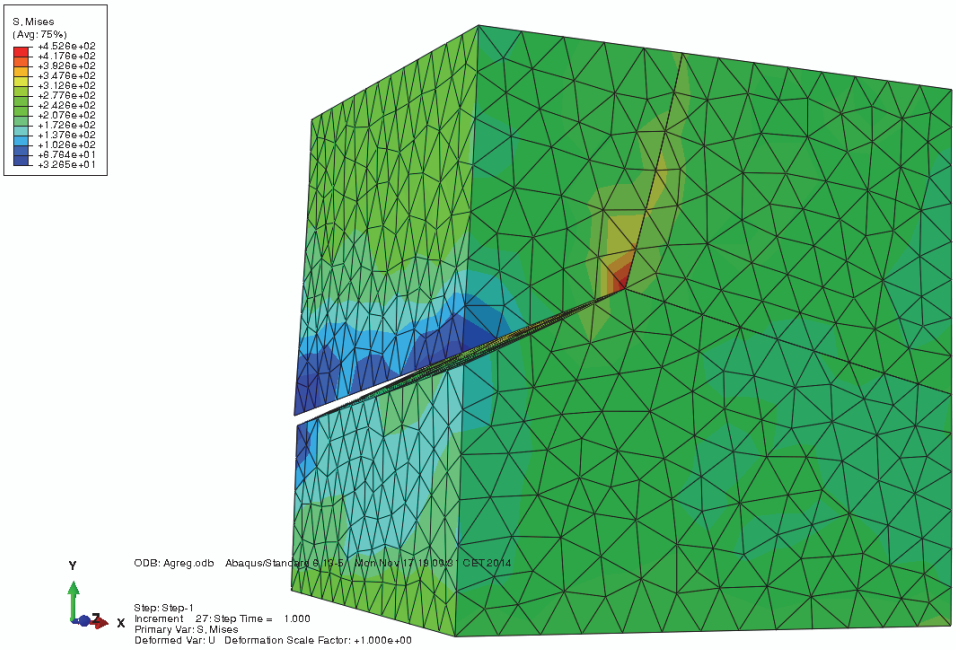

Figure 7: 10% deformed 3D-voronoï aggregate generated using Neper with a debound surface stopped at a triple line (preliminary result) [13]

CONCLUSION

LME in the case of steels is conclusively shown here to consist in many cases of intergranular or interlath cracking. One often overlooked issue is the interplay between fracture and local plasticity making fracture surface often difficult to clearly assign to a microstructural element of the material. We have conclusively shown in this work that fractography needs to be completed with state-of-the-art nanoscale characterization tools (FIB sampling, EBSD,

tEBSD). The information gained is qualitatively important since we now know that we have to deal with an intergranular cracking phenomenon. The modeling of this class of LME cases involves a full field description of the 3D microstructure coupled with crystalline plasticity. LME fracture criteria will be able to be compared with experimental results within such a framework in a future work.

REFERENCES

[1] Nicholas, M.G., Old, C.F., Review Liquid metal embrittlement, Journal of Materials Science, 14 (1979) 1-18.
[2] Coen, G., Van den Bosch, J., Almazouzi, A., Degrieck, J., Investigation of the effect of lead-bismuth eutectic on the fracture properties of T91 and 316L, Journal of Nuclear Materials, 398 (2010) 122-128.
[3] Skeldon, P., Hilditch, J.P., Hurley, J.R., Tice, D.R., The liquid metal embrittlement of 9Cr steel in sodium environments and the role of non-metallic impurities, Corrosion Science, 36 (1994) 593-610.
[4] Lynch, S.P., A fractographic study of gaseous hydrogen embrittlement and liquid-metal embrittlement in a tempered-martensitic steel, Acta Metall., 32 (1984) 79-90.
[5] Lynch, S.P., Metallographic contributions to understanding mechanisms of environmentally assisted crackingMetallography, 23 (1989) 147-171.
[6] Martin, M.L., Auger, T., Johnson, D.D., Robertson, I.M., Liquid-metal-induced fracture mode of martensitic T91 steels, Journal of Nuclear Materials, 426 (2012) 71-77.
[7] Hamdane, O., Proriol-Serre, I., Vogt, J.B., Nuns, N., ToF-SIMS analyses of brittle crack initiation of T91 steel by liquid sodium, Materials Chemistry and Physics 145, (2014) 243-249.
[8] Hémery, S., Auger, T., Courouau, J.-L., Balbaud-Célérier, F., Liquid metal embrittlement of an austenitic stainless steel in liquid sodium, Corrosion Science, 83 (2014) 1-5.
[9] Hémery, S., Auger, T., Courouau, J.-L., Balbaud-Célérier, F., Effect of oxygen on liquid sodium embrittlement of T91 martensitic steel, Corrosion Science, 76 (2013) 441-452.
[10] Hilditch, J.P., Hurley, J.R., Skeldon, P., Tice, D.R., The liquid metal embrittlement of iron and ferritic steels in sodium, Corrosion Science, 37 (1995) 445-454.
[11] Legris, A., Nicaise, G., Vogt, J.-B., Foct, J., Liquid metal embrittlement of the martensitic steel 91: influence of the chemical composition of the liquid metal: Experiments and electronic structure calculations, Journal of Nuclear Materials, 301 (2002) 70-76.
[12] J. Kargol, A., Albright, D.L., The effect of relative crystal orientation on the liquid metal induced grain boundary fracture of aluminum bicrystals, Metallurgical Transaction A, 8 (1977) 27-34.
[13] Quey, R., Dawson, P.R., Barbe, F., Computer Methods in Applied Mechanics and Engineering, 200 (2011) 1729-1745.
[14] Simonovski, I., Cizelj, L., Computational Materials Science, 50 (2011) 1606-1618.
[15] Rey, C., Fandeur, C., Simulation par la méthode des éléments finis du comportement mécanique local des polycristaux. Couplages physiques. ECP SCIENCE. Rayonnement synchrotron rayons X et Neutrons au Service des Matériaux, ECP Sciences ed., (2013) 410-448.
[16] Schwartz, J., PhD thesis, ECP, France, (2010).
[17] Peirce, D., Asaro, R.J., Needleman, A., Material rate dependence and localized deformation in crystalline solids, Acta Metall., 31 (1983) 1951-1976.
[18] Tabourot, L., Fivel, M., Rauch, E., Generalised constitutive laws for fcc single crystals, Mat. Sci. Eng. A, 234 (1997) 639-642.
[19] Erieau, P., Rey, C., Modelling of deformation and rotation bands and of deformation induced grain boundaries in IF Steel aggregate during large plane strain compression, International Journal of Plasticity, 20 (2004) 1763-1788.
[20] Griffith, A.A., The Phenomena of Rupture and Flow in Solids, Phil. Trans. R. Soc. Lond., A 221 (1921) 163-198.
[21] Hirth, J.P., Rice, J., On the Thermodynamics of Adsorption at Interfaces as it Influences Decohesion, Metallurgical Transactions A, 11A (1980) 1501-1511.